Stability and mixing behavior of vanadium-iron oxide monolayers on Pt(111) and Ru(0001) substrates

Jacek Goniakowski, Piotr Igor Wemhoff, Niklas Nilius, Claudine Noguera

Stability and mixing behavior of vanadium-iron oxide monolayers on Pt(111) and Ru(0001) substrates

J. Goniakowski[a], P. I. Wemhoff[b], N. Nilius[b], C. Noguera[a]

[a]CNRS-Sorbonne Université, UMR 7588, INSP, F-75005 Paris, France ‡
[b]Carl von Ossietzky Universität, Institut für Physik, D-26111 Oldenburg, Germany §

Abstract. Cation mixing is a well-recognized mean to obtain oxides of desired functionality with predetermined structure and stoichiometry, which yet has been only little analyzed at the nanoscale. In this context, we present a comparative analysis of the stability and mixing properties of O-poor and O-rich two-dimensional V-Fe oxides grown on Pt(111) and Ru(0001) surfaces, with the aim of gaining an insight into the role of substrate and oxygen conditions on the accessible Fe contents. We find that due to the high oxygen affinity of the Ru substrate, the mixed O-rich layers are highly stable while the stability of O-poor layers is limited to inaccessibly oxygen-poor environments. In contrast, on the Pt surface, O-poor and O-rich layers coexist with, however, a much lower Fe content in the O-rich phase. We show that cationic mixing (formation of mixed V-Fe pairs) is favored in all considered systems. It results from local cation-cation interactions, reinforced by a site effect in O-rich layers on the Ru substrate. In O-rich layers on Pt, Fe-Fe repulsion is so large that it precludes the possibility of substantial Fe content. These findings highlight the subtle interplay between structural effects, oxygen chemical potential, and substrate characteristics (work function and affinity towards oxygen), which governs the mixing of complex 2D oxide phases on metallic substrates.

‡ e.mail: jacek.goniakowski@insp.jussieu.fr, claudine.noguera@insp.jussieu.fr
§ e.mail: piotr.igor.wemhoff@uni-oldenburg.de, niklas.nilius@uni-oldenburg.de

1. Introduction

The exceptional versatility of oxide compositions, structures and properties is nowadays increasingly recognized in many modern technologies. Oxide materials are present in microelectronic devices, as transparent layers in optical coatings and solar energy harvesting devices, as protective layers against corrosion of metals, and as efficient catalysts in many important chemical reactions [1, 2, 3, 4].

Changing oxygen thermodynamic conditions during synthesis is a robust lever to obtain oxides of predetermined characteristics, a key requirement for an efficient fabrication of nanoscale materials [5, 6, 7]. A particularly large range of structures and stoichiometries has been observed in various two-dimensional (2D) oxide nanolayers obtained under different oxygen partial pressures and/or annealing temperatures during their deposition on metal substrates or during oxidizing the substrate itself. Illustrative examples are AlO_x monolayers (MLs) formed on NiAl or FeAl alloys [8, 9], CuO_x on Cu(111) [10], or Au(111) [11], MnO_x formed on Pd(100) [12], VO_x MLs on Rh(111) [13], TiO_x MLs on Pt(111) [14], FeO_x MLs on Pt(111) [15, 16], Pd(111) [17] and Ag(100) [18] or CoO_x MLs on Pt(111) [19]. Among the numerous synthesized phases, many have no bulk equivalents and display specific crystalline structures, which paves the way to the fabrication of completely new materials with tailored electronic, magnetic, optical, or chemical properties. Moreover, film properties can be further tuned by the choice of the metal support with which electron transfers and chemical interactions may take place.

Structural and compositional flexibility of oxide films can be significantly extended by combining different cations, a strategy extensively developed in mixed bulk oxides, such as ordered perovskites, spinels, etc, or disordered solid solutions [20, 21, 22]. Studies of well-characterized mixed 2D oxide layers are much scarcer. Recent examples include thin oxide films based on the intermixing of Si-Al [23], Si-Li [24], Ti-Ba [25, 26, 27], Mo-Ca [28], Ni-W [29], and Co-Fe [30], among others. In recent density function theory (DFT) works, we have studied mixing properties in model 2D mixed oxide honeycomb (HC) MLs, whether free-standing [31] or supported on metal substrates [32, 33]. We have evidenced how they vary as a function of the band off-sets between the various components (oxide parents and/or substrate) via changes of the cation oxidation states and we have stressed the key role of the film low dimensionality. Furthermore, since cation distribution in such systems may be determined using surface science tools such as high-resolution scanning tunneling microscopy (STM), in the case of 2D mixed V-Fe oxide layers on Pt(111) [34] and Ru(0001) [35] substrates, we have successfully synthesized and finely characterized ultra-thin films with different proportions of the two cations.

The present work is devoted to a comparative analysis of the stability and mixing characteristics of O-poor and O-rich mixed V-Fe oxide ultra-thin films which have been observed on the Pt(111) and Ru(0001) surfaces. We demonstrate that their properties result from a subtle interplay between structural effects, oxygen chemical potential, and substrate characteristics (work function and affinity towards oxygen).

The manuscript is organized in the following way. After a description of experimental and theoretical methods in Section 2, experimental results on the mixed layers are summarized (Section 3). Theoretical results are reported in Section 4, and discussed in Section 5, before concluding (Section 6).

2. Experimental and theoretical methods

The experiments have been performed in an ultrahigh vacuum chamber ($p \approx 2 \times 10^{-10}$ mbar base pressure), enclosing a liquid-nitrogen cooled STM, a low-energy electron diffraction (LEED) setup as well as standard tools for sample cleaning and thin film preparation. All STM data were acquired in the constant current mode with electrochemically etched Au tips. The mixed oxide layers were grown on two single crystalline surfaces, Pt(111) and Ru(0001), cleaned by cycles of Ar^+ sputtering and annealing. The actual film preparation comprised three steps: (i) vacuum deposition of 0.05 to 0.3 ML Fe, (ii) 0.3 ML V deposition in 1×10^{-6} mbar oxygen ambience, (iii) film crystallization at 600 K either in 2×10^{-10} (UHV) or in 1×10^{-6} mbar O_2 (O-rich conditions) to fabricate films with different oxygen content. A first check of the integral film quality was realized by LEED, whereby a sharp (2×2) superstructure pattern evolved after formation of well-ordered oxide honeycomb films on both substrates (see Supporting Information, section S1). Note that excessively O-rich or Fe-rich preparations could be readily identified at

this stage due to their deviating LEED patterns.

DFT calculations were performed with the Vienna Ab-initio Simulation Package (VASP) [36, 37] using the Projector Augmented Wave (PAW) method [38, 39] to represent the electron-core interaction and a 400 eV energy cut-off in the development of Kohn-Sham orbitals on a plane-wave basis set. We have checked that an increase of the cut-off to 500 eV does not bring any noticeable modifications to the reported results. A dispersion-corrected exchange-correlation functional (optB88-vdW) [40, 41, 42] was employed, within the DFT+U approach proposed by Dudarev at al. [43, 44] As in our previous studies [31, 32, 45, 46], we have used U values close to those reported in the literature: U_V = 1.7 eV and U_{Fe} = 3 eV. All calculations were spin-polarized and the relative stability of simple non-magnetic (NM) and magnetic solutions (with either parallel (FM) or anti-parallel (AF) spin moments) was systematically tested. Ionic charges were estimated with the partition scheme proposed by Bader [47, 48] and magnetic moments were obtained by integration of the spin density within the Bader's volumes. Atomic configurations were plotted with VESTA [49].

We have considered pure and mixed $(V_{1-c}Fe_c)_2O_n$ layers in either a (4×4)-Ru(0001) or a $(2\sqrt{3}\times2\sqrt{3})$-Pt(111) surface unit cell at the experimental in-plane bulk lattice parameter (2.705 Å and 2.765 Å, for Ru and Pt, respectively). The oxygen content n was varied between 3 and 7 and $0 \leq c \leq 0.5$ is the Fe concentration in the layers. The sampling of the Brillouin zones was performed with the Γ-centered (2×2) and (3×3) Monkhorst-Pack mesh [50], respectively. The metal substrates were represented by slabs composed of four atomic planes, the oxide layers were deposited on one side of metal slabs, and dipole corrections were applied. All atomic coordinates of anions, cations, and surface metal atoms have been allowed to fully relax until forces got lower than 0.01 eVÅ^{-1}. Apart from the bottom metal layer that was kept in its bulk position, atoms in the subsurface metal layers were allowed to relax only perpendicularly to the surface. We checked that an addition of a fifth metal layer resulted in only negligible corrections on the reported quantities.

All formation energies, E_{form} (per cation), were calculated with respect to corundum Fe_2O_3 and rutile VO_2 which represent the two pure oxide bulk phases stable in a wide range of oxygen conditions (-2.6 eV < $\Delta\mu_O$ < -1.1 eV), including those relevant for the experiments (-1.6 eV < $\Delta\mu_O$ < -1.1 eV), according to:

$$\begin{aligned} 2E_{form} = E((V_{1-c}Fe_c)_2O_n/Me) - E(Me) \\ -2(1-c)E(VO_2) - cE(Fe_2O_3) \\ -(n-4+c)(\frac{1}{2}E(O_2) - \Delta\mu_O) \end{aligned} \quad (1)$$

Here $E((V_{1-c}Fe_c)_2O_n/Me)$, $E(Me)$, $E(VO_2)$, $E(Fe_2O_3)$, and $E(O_2)$ refer to the energies of the supported film, the metal substrate (Me = Pt, Ru), one formula unit of bulk VO_2 and Fe_2O_3, and an oxygen molecule, respectively. The bulk VO_2 and Fe_2O_3 energies approximate well energies of either thick films or large clusters of the two pure oxides which might form at the metal substrates as an alternative to the observed mixed monolayers.

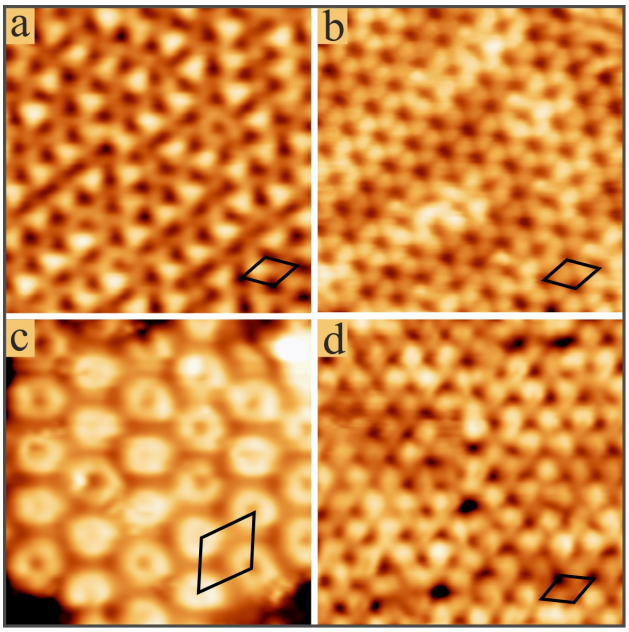

Figure 1. STM topographic images (5×5 nm^2) of V-Fe mixed oxide films post-annealed in UHV on (a) Pt(111) (U_B = 1.4 V) and (b) Ru(0001) (U_B = 0.3 V) and at 1×10^{-6} mbar O_2 on (c) Pt(111) (U_B = 0.3 V) and (d) Ru(0001) (U_B = 0.5 V).

3. Experimental results

This section describes the main characteristics of the mixed layers which have been synthesized under UHV and O-rich oxygen conditions on Pt(111)and Ru(0001). Large scale STM images of the layers on Pt(111) and Ru(0001) are shown in the Supporting Information (SI), Section S1, Fig. S1 and S2. In the following we present and discuss high resolution STM images of these layers. We will show that, while the change of oxygen conditions has no impact on the oxide film grown on Ru(0001), distinctly different layer structures and compositions are observed on Pt(111).

More precisely, under UHV annealing conditions, two characteristic mixed oxide configurations are detected experimentally, one on Pt(111) and one on Ru(0001). The Pt(111)-supported film crystallizes in a simple honeycomb lattice in (2×2) registry with respect to the metal [34]. Embedded Fe atoms in the film are readily identified by their bias-dependent contrast and distinct triangular shapes in atomically resolved STM data (Fig. 1a). Whereas Fe appears

with lower apparent height than V at negative and small positive bias, it dominates the contrast above +1.0 V sample bias. Responsible for this contrast switch is the Fe $3d_{z^2}$ orbital that carries a large portion of the tunneling current at high bias. The STM image in Fig. 1a was taken in this regime, so that the Fe content of the $(V_{1-c}Fe_c)_2O_3$ honeycomb film could be determined to $c = 0.28$ simply by counting the bright, triangular features. By varying the Fe exposure time, the concentration of embedded iron could be changed between $0 < c < 0.5$. At higher Fe exposure, designated Fe-rich oxide phases emerge on the surface, most prominently a FeO bilayer phase. The topographic elevation of the mixed $(V_{1-c}Fe_c)_2O_3$ honeycomb film amounts to 1.5 Å above the Pt(111) surface at 0.25 V, a value that shows only little bias dependence.

Under the same preparation conditions, the mixed oxide film on Ru(0001) also crystallizes in a honeycomb lattice with (2×2) registry. In contrast to the Pt(111) support, the honeycomb grows in hexagonal domains of 3-5 nm size, delimited by grain boundaries along which the 6-cation honeycomb rings are replaced by sequences of 5-, 8- and 9-membered rings. This boundary network enables the film to compensate the lattice mismatch with the Ru(0001) surface. Whereas the V-Fe honeycomb lattice is readily detected in low-bias STM measurements (Fig. 1b), the contrast converts to a (2×2) pattern with every second cation showing up at higher bias. This contrast difference between bright and dark species is however unrelated to the chemical identity of the cations, but governed by their binding geometry on the Ru(0001) support. In fact, no contrast signatures could be derived for V and Fe species from bias-dependent STM images, which renders their distinction difficult from experimental data alone. Nonetheless, the film stoichiometry was elucidated in combination with DFT calculations, finding an almost equal distribution of V and Fe cations [35]. Small deviations from the one-to-one stoichiometry give rise to point defects in the honeycomb lattice, either Fe → V substitutions or Fe interstitials in the rings centers for Fe-poor and Fe-rich compositions. Larger deviations from a balanced V to Fe distribution immediately initiate a phase separation, in which mixed V-Fe honeycomb patches develop together with VO_x and FeO binary phases for V and Fe excess, respectively [51, 35]. Apart from the effect of stoichiometry self-organization, also the topographic height of mixed honeycomb oxides differs distinctively on Pt(111) and Ru(0001) supports. In the latter case, a height of 3.0 Å is measured independent of bias voltage, almost twice the value of the Pt(111)-grown film.

Switching to more O-rich conditions (annealing at 1×10^{-6} mbar O_2) hardly changes the appearance of mixed oxide films on Ru(0001), as exemplified in Fig. 1d. In fact, all structural and morphological parameters are similar to the ones obtained under UHV conditions, as shown in panel (b). More precisely, the film height (3.0 Å), the periodicity of the honeycomb lattice (5.4 Å) and the relaxation network are indistinguishable for both preparations, suggesting that identical mixed oxide configurations develop on Ru(0001) in both regimes.

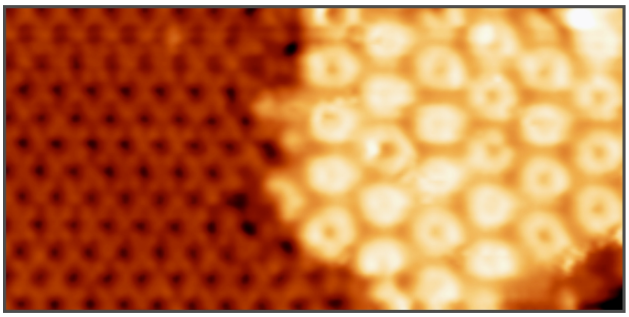

Figure 2. STM topographic image of a V-Fe mixed oxide film on Pt(111) prepared at O-rich conditions. While the characteristic O-poor phase is detected on the left, the coexisting O-rich phase is seen on the right part of the image (10×5 nm^2, U_B = 0.3 V).

A completely different situation is encountered for O-rich oxide preparations on Pt(111). Here, a plethora of new oxide phases is observed, including amorphous 2D oxide patches, stripes of variable width running along Pt⟨110⟩ and hexagonal patterns of different periodicity. In this work, we concentrate on the most simple, hexagonal structure that mimics the symmetry of the honeycomb lattice discussed before, while the more complex mixed oxide films will be subject of a forthcoming paper. A high-resolution STM topography of the hexagonal V-Fe mixed oxide prepared in O_2 excess is depicted in Fig. 1c. The new phase always coexists with the honeycomb film discussed before (Fig. 2), suggesting similar formation energies at the selected experimental conditions. The O-rich film consists of ring-like features with 6 Å diameter, similar to the honeycomb size, and 9.5 Å periodicity. The latter corresponds to $\sqrt{3}$ times the unit cell size of honeycomb films, in agreement with a 30° rotation between the two structures. Moreover, not all rings are fully identical and filled and empty pores can be distinguished, probably due to the filling of some rings by foreign atoms. As for the Ru-supported layer, distinction between Fe and V atoms, e.g. via bias-dependent topographic measurements, turned out to be impossible. However, the fact that this phase is not observed in the absence of Fe points towards its mixed V-Fe character. The low-bias topographic height of the O-rich mixed oxide on

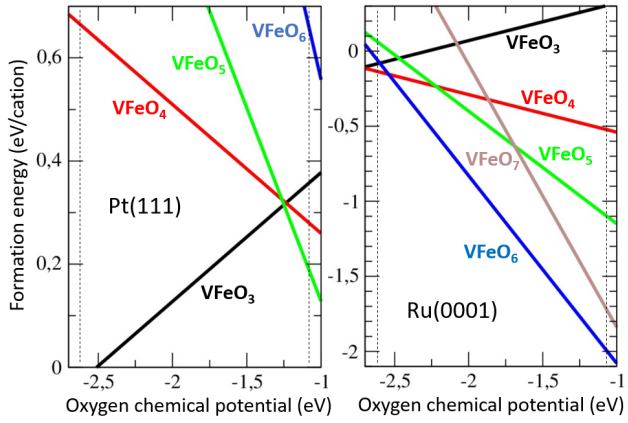

Figure 3. Formation energies of metal-supported mixed $VFeO_n$ honeycomb films with various oxygen contents, n = 3 - 7, as a function of oxygen chemical potential. Dashed lines indicate the calculated stability limits of the bulk VO_2 phase.

Pt(111) is measured to 2.5 Å , being ≈1 Å higher than its O-poor counterpart.

4. Theoretical results

As a first step, we have estimated the relative stability of metal-supported oxide films with a 6-cation ring structure and a V/Fe cation ratio of 1:1 (c = 0.5). More precisely, starting from the simplest mixed $VFeO_3$ HC film deposited on the two metal substrates, we have constructed a series of $VFeO_n$ (n = 4 - 7) configurations by successive addition of oxygen. Different configurations have been considered for each stoichiometry, with O atoms added either on top of the oxide film or at the oxide/metal interface. Various offsets between the substrate, the interfacial oxygen atoms, and the oxide layer have been tested. The most stable structures for each stoichiometry are displayed in Fig. S3 and S4 in the Supporting Information (SI, section S2). Figure 3 depicts the relative stability of these configurations for each oxygen content in a range of oxygen chemical potentials largely exceeding the experimental one.

Regarding the relative phase stability as a function of the oxygen content, the dependence of E_{form} on $\Delta\mu_O$, according to Eq. 1, is driven by the sign of the factor $n - 4 + c$ which is negative for $VFeO_3$ (n = 3) and positive for all the other phases, whatever $0 < c < 0.5$. The consequence is that O-poor/O-rich layers are destabilized/stabilized when the thermodynamic conditions become more and more oxygen-rich, as shown in Fig. 3 and as expected.

On both substrates only two phases, one O-poor and one O-rich, are predicted to be thermodynamically stable in a significantly large span of oxygen conditions. On the Pt(111) surface, an O-poor $VFeO_3$ phase is the most stable for $\Delta\mu_O$ < -1.3 eV, whereas an O-rich $VFeO_5$ one is favored for $\Delta\mu_O$ > -1.3 eV. On the Ru(0001) surface, a similar $FeVO_3$ phase is favored for $\Delta\mu_O$ < -2.7 eV, and a more oxygen-rich, $VFeO_6$ one, for $\Delta\mu_O$ > -2.6 eV. The difference in the transition point on the two substrates (extremely O-poor on Ru and experimentally accessible on Pt) is consistent with the experimental finding of the coexistence of two phases on Pt, Fig. 2, whereas only the O-rich phase has been observed on Ru [35]. The difference can be traced back to a different stability of the O-rich phases. Indeed, while the formation energies of the two $VFeO_3$ phases remain quite similar for both substrates (0.0 - 0.4 eV/cation in the considered range of $\Delta\mu_O$), those of the two O-rich phases differ by roughly 2 eV. The formation energy of $VFeO_6$/Ru is systematically more negative than that of $VFeO_5$/Pt, thus shifting the transition point towards extremely O-poor conditions. The enhanced stability of the O-rich film on Ru may be assigned to its larger oxygen content and its stronger interaction with the substrate due to the Ru high oxygen affinity.

Apart from the precise Fe content in each phase which will be analyzed in the following, it is worth noting that the predicted film structures (Fig. 4) correspond well to those observed experimentally (a more detailed account is given in Refs. [34, 35] and the whole set of new oxide phases observed for O-rich conditions on Pt(111) will be described in a forthcoming paper). The only exception is the $VFeO_3$/Ru(0001) film which requires much more O-poor oxygen conditions than experimentally achieved and could not be observed. Nevertheless, we will include it in the following analysis for the sake of comparison with the other systems.

The two O-poor phases correspond to a simple $VFeO_3$ honeycomb film (Fig. 4top panels) with electronic and structural characteristics typical for this class of materials [7, 33]. Namely, cations and anions are 3-fold and 2-fold coordinated, respectively. The former are located close to the hollow sites of the metal surfaces, and the latter approximately on top of the surface metal atoms. Anions relax outward with respect to cations, which gives rise to a noticeable film rumpling of about 0.7 and 0.8 Å on Pt and Ru, respectively. The film structure is somewhat more complex in the case of the Ru substrate, where one among the three oxygen atoms relaxes slightly inwards and forms a Ru-O bond with the substrate. The electronic structures of such HC monolayers, Tab. 1, are characterized by an electron transfer from the oxide films toward the metal substrates. This electron transfer is larger in the case of Pt and results in an increase of the vanadium oxidation state, as witnessed by its large Bader charge Q_V and by its

Table 1. Main Electronic Characteristics of the Metal-supported $VFeO_n$ Films: Cation Bader Charges Q_V , Q_{Fe} (e), and Magnetic Moments μ_V, μ_{Fe} (μ_B), and Total Charge of the Metal Substrate Q_{sub} (e/$VFeO_n$ f.u.)

	$VFeO_3$/Pt	$VFeO_5$/Pt	$VFeO_3$/Ru	$VFeO_6$/Ru
Q_V, Q_{Fe}	1.95, 1.49	2.15, 1.76	1.80, 1.29	2.08, 1.69
μ_V, μ_{Fe}	0.1, 3.9	0.2, 4.0	0.1, 3.7	0.1, 4.0
Q_{sub}	-0.70	+0.68	-0.17	+1.71

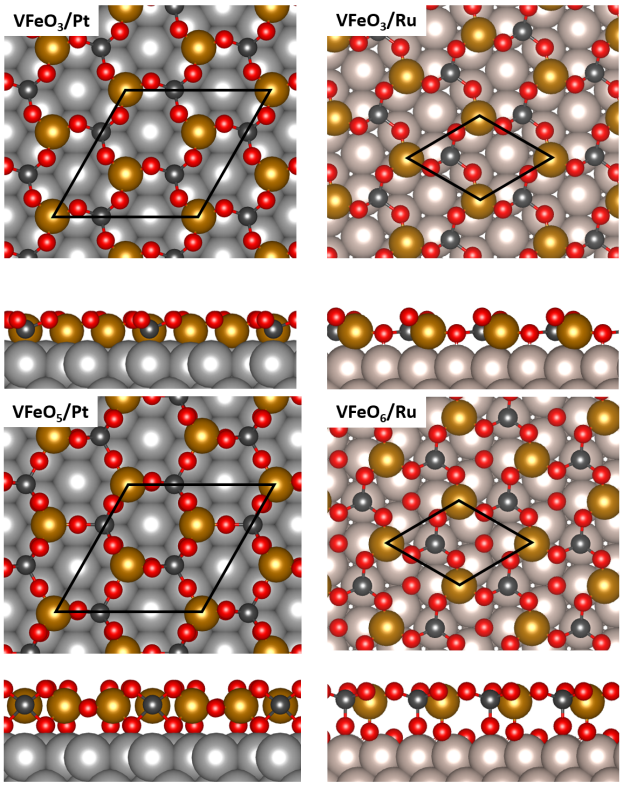

Figure 4. Top panels: Top and side views of the atomic structures of the O-poor $VFeO_3$/Pt(111) and $VFeO_3$/Ru(0001) honeycomb mixed oxide films. Bottom panels: Top and side views of the atomic structures of the O-rich $VFeO_5$/Pt(111) and $VFeO_6$/Ru(0001) mixed oxide films. V, Fe, O, Pt, and Ru atoms are plotted with black, golden, red, gray and light brown balls, respectively.

quenched magnetic moment μ_V [34]. On Ru, the overall electron transfer is smaller, because it has two opposing components. First, similarly to the Pt case, the oxide to metal component enhances the oxidation state of vanadium. Second, due to the Ru-O bond formed across the interface, an electron transfer takes place in the opposite direction, which reduces the overall negative charge of the Ru substrate.

The two O-rich phases contain additional oxygen atoms at the interface. They display quite different atomic structures and different oxygen contents on the two substrates. On the Pt(111) surface (Fig. 4 left bottom panel), the two interfacial oxygen atoms are located on top of surface Pt atoms. Each of them forms two bonds with the cations in the oxide film, thus producing a structure akin to a trilayer, and an additional one with the Pt surface. As a consequence, cations which are located in the hollow sites of the metal surface are 5-fold coordinated.

On the Ru(0001) surface (Fig. 4 right bottom panel), the three interfacial oxygen atoms are strongly bonded to the Ru surface atoms, in either top (O_A atoms) or hollow sites (O_B and O_C atoms). O_A and O_B form a single bond with V and Fe cations, respectively, which are thus in a distorted tetrahedral environment. The O_C atom has no link to the oxide layer and can be seen as reminiscent of the ordered oxygen overlayers that evolve on pure Ru(0001) under similar oxygen conditions.

The electronic characteristics of the O-rich films ($VFeO_5$/Pt(111) and $VFeO_6$/Ru(0001)) are consistent with maximal formal oxidation states of the two cations (V^{5+} and Fe $^{3+}$) [35], driven by the large oxygen content in the film. Stabilization of the excess oxygen with respect to the charge-neutral $V^{5+}Fe^{3+}O_4^{2-}$ oxide formula unit (1 excess oxygen atom on Pt and 2 on Ru) is due to the interaction with the metal substrates. It occurs via the formation of interfacial Pt-O or Ru-O bonds and an electron transfer toward the oxide layer. It results in an overall positive charging of the metal substrate. A similar stabilization mechanism has been already proposed for O-rich FeO_2 films on the Pt substrate [15, 16].

As a whole, the differences between structure and stoichiometry of the O-rich mixed oxide phases on the two substrates result from the higher oxygen affinity of Ru, compared to Pt, which drives both the oxygen content and the cation local environment in the layers.

In a second step, we have re-evaluated the stability of the O-poor and O-rich phases for each substrate, this time as a function of the V/Fe cation ratio in the films. More precisely, starting from the pure V_2O_n films ($n = 3$ for O-poor phases on both Pt and Ru; $n = 5$ and 6 for O-rich phases on Pt and Ru, respectively), we considered an increasing number of Fe substitutions in the (4×4)-Ru(0001) or ($2\sqrt{3}$×$2\sqrt{3}$)-Pt(111) unit cells. This leads to unit cell contents $V_{6-m}Fe_mO_9$ and $V_{6-m}Fe_mO_{15}$ on Pt for O-poor and O-rich phases, respectively (Fe concentrations $c = m/6$). Corresponding layer compositions on Ru are $V_{8-m}Fe_mO_{12}$ and $V_{8-m}Fe_mO_{24}$ (Fe concentrations $c = m/8$). Various Fe distributions in the 6-cation

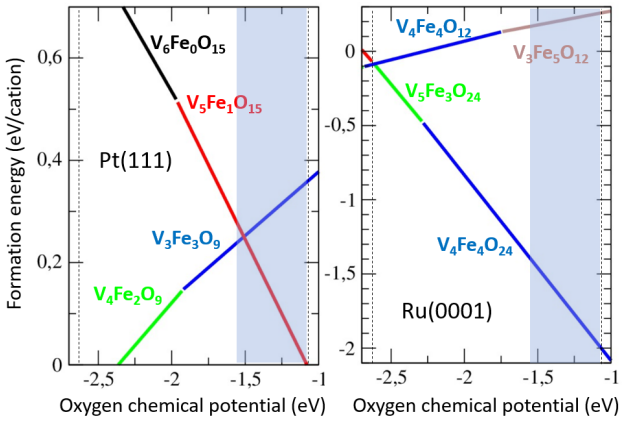

Figure 5. Formation energies of metal-supported O-poor and O-rich films with different Fe contents, as a function of oxygen chemical potential. Dashed lines indicate the calculated stability limits of the bulk VO_2 phase. Shaded region highlights oxygen conditions relevant to the present experiments.

rings have been considered for each Fe content and their alternative positions with respect to the metal substrate were also tested. Fig. 5 depicts the formation energies of the most stable configurations in a grand canonical approach which assumes that an unrestricted number of vanadium and iron atoms is available from bulk oxide reservoirs. Under Fe dosing control, the composition c of the layers could be more freely varied, as demonstrated in our previous work on O-poor mixed layers on Pt [34].

We find that moving from O-poor to O-rich oxygen conditions produces a systematic increase of the favored Fe content in both O-poor and O-rich phases, Fig. 5. This trend is driven by the term $-c\Delta\mu_O$ in Eq. 1. However, the optimal c value differs in the four phases. Under experimentally relevant oxygen conditions (shaded region), mixed oxide phases of compositions close to 1:1 are favored in three among the four systems under consideration. The only exception is the O-rich $(V_{1-c}Fe_c)_2O_5$/Pt film, for which the favored Fe content is much smaller. In the most stable configurations, the Fe cations are systematically located in 2nd neighbor positions with respect to each other (Fig. 4), while configurations involving first-neighbor Fe-Fe pairs are considerably less stable. This shows a systematic preference for the formation of mixed V-Fe pairs rather than of pure V-V and Fe-Fe ones. We will analyze the mechanisms responsible for these features in the Discussion section.

Let us finally note that simulated STM images of the three most stable films in the experimentally accessible range of oxygen chemical potentials are in excellent agreement with the experimental images shown in Figs. 1 and 2. As presented in Fig. S5, Section S3 of the SI, on Pt(111), under UHV annealing conditions, Fe atoms can be recognized by their triangular motif at high bias. On Ru(111), the STM contrast is driven by the height of the cations linked to O_A interfacial oxygen atoms and not to the chemical identity of the cations. Finally, on Pt(111) under more oxygen rich conditions, the STM contrast is determined by the outermost oxygen atoms, and all cation positions in the six-ring show up by small depressions in the ring circumference. There is negligible contrast due to the chemical identity of the cations.

5. Discussion

The experimental and theoretical results described in the previous sections evidence several important characteristics of the O-poor and O-rich mixed V-Fe oxide 2D layers on Pt(111) and Ru(0001). The most stable configurations have a honeycomb-type structure with alternating V and Fe cations within the 6 cation-membered rings and interfacial oxygen atoms in the case of O-rich layers. A mixing of the two cations thus takes place at the atomic level, with a preference for V-Fe rather than V-V or Fe-Fe first neighbor pairs. Despite this common feature, the O-rich layers on Pt depart from the other systems by a much lower optimal Fe content, and the O-rich layers on Ru(0001) by a much larger stability. In this section, we propose some guidelines to rationalize these characteristics.

The usual way to analyze the mixing behavior of a substitutional alloy consists, at T=0 K, in evaluating its mixing energy as the difference between its energy and the energy of its end-members weighted by their relative concentrations. This procedure has been widely applied for metallic alloys [52], simple oxides [53, 54], as well as mineral compounds [55]. An important condition is that the two end-members have the same crystalline structure and stoichiometry. However, in the present case, most end-members (Fe_2O_3, Fe_2O_5, V_2O_5, V_2O_6, and Fe_2O_6) are not the most stable binary oxide phases on Pt and Ru in the considered range of oxygen chemical potentials. Indeed, on the Pt(111) substrate, O-poor FeO and O-rich FeO_2 phases have been experimentally observed [15, 16], whereas on Ru(0001), the observed Fe-rich structures have been interpreted as FeO bilayers [56, 57, 58]. In the three cases, the building elements of the structure are small 3-cation rings, while the mixed layers described here display larger 6-cation rings. Similarly, on Ru, the most stable oxygen-rich pure vanadium oxide displays rings which involve more than 6 cations [51]. It thus appears that, in complex systems such as 2D mixed layers on metal substrates, due to the flexibility of their structures and compositions when the thermodynamic conditions change, the traditional way of quantifying mixing properties is not applicable

and has to be reconsidered.

In order to circumvent this difficulty and characterize the cation distribution in the unit cells, we have calculated the energy costs δE_i to approach two Fe cations at various relative positions (i=1, 2... for first, second.... neighbor positions) and with alternative (FM or AF) spin orientations, as described in Ref. [34]. Since this process conserves the number of vanadium, iron and oxygen atoms, the δE_i are independent of all chemical potentials, i.e. $\Delta\mu_O$ and the bulk references. Values for δE_1 and δE_2 are given in Table 2.

Within an Ising-type model, the δE_i quantities may be written as a function of (1) effective cation-cation interactions W_i weighted by a number of mixed pairs n_i, and of (2) a site energy term ΔE whenever first ($i = 1$) or third ($i = 3$) neighbor V-Fe pairs are involved:

$$\delta E_i = -n_i W_i + (\delta_{i,1} + \delta_{i,3})\Delta E \quad (2)$$

The meaning of the ΔE and W_i parameters is presented and discussed in the following. Their values are given in Table 2. Considering that they somewhat vary with the Fe concentration, we will only discuss their most salient features which are independent on c.

Regarding the site term ΔE, one may note that the cationic sites along the 6-membered rings are not equivalent. For example, in the O-poor layers, cations alternatively occupy two different hollow sites of the substrate. DFT calculations performed on configurations with a single Fe atom in the unit cells, find that the energy ΔE to exchange V and Fe cations located on sites of different type does not exceed a few hundredth of eV. In the O-rich layers, ΔE is larger, especially on Ru. As discussed in Ref. [35], in this case, cations are located on-top of interfacial oxygen atoms which are either top (O_A sites) or hollow (O_B sites) of the Ru surface. O_A and O_B sites alternate along the rings and O_A is much more favourable for V cations because it allows stronger V-O bonds to be formed. This site effect effectively favours V-Fe first neighbor pairs, by approximately 0.6 eV, and leads to an optimal mixing behavior at $c = 0.5$. It provides the major contribution to δE_1 for O-rich layers on Ru, while for O-rich layers on Pt, it is insufficient to explain a nearly as high δE_1 value. Moreover, in the latter case, it nearly completely vanishes as the Fe concentration increases.

The mixing parameters $W_i = 2E_i^{FeV} - E_i^{FeFe} - E_i^{VV}$ are related to effective pair interaction energies E_i^{FeV}, E_i^{FeFe} and E_i^{VV}. They account for the energy gain (or expense) to form two Fe-V pairs in place of one Fe-Fe and one V-V pair (at a given distance i). Negative and positive W values are indicative for mixing (preference for Fe-V pairs) and phase separation (preference for Fe-Fe and V-V pairs), respectively. Let us note that, since negative W values favor V-Fe pairs at the expense of Fe-Fe and V-V ones, they represent effective V-Fe attraction as well as Fe-Fe or V-V repulsion. According to Table 2, first neighbor parameters W_1 are rather large and negative in all mixed layers, which indicates local mixing of the two cations at the atomic level. Second neighbor parameters W_2 are comparatively small, whereas third neighbor ones can be neglected.

Yet, the comparison between the W_i values in the four systems evidences the specificity of the O-rich layers on Pt which possess both the largest W_1 and the largest W_2 parameters, which, among the four systems, results in a high energy costs δE_1 and the highest one δE_2 to approach two Fe cations in first of second neighbor positions, respectively. As introducing more and more Fe atoms in the layers inevitably creates second- or even first-neighbor Fe-Fe pairs and thus increases the Fe-Fe repulsion, it prevents the stabilisation of O-rich phases on Pt with a substantial Fe content. Actually already an isolated V-Fe substitution costs more energy than in the other systems due to the larger number of strong V-O bonds which are replaced by weaker Fe-O ones (five in O-rich layers on Pt, and three/four in O-poor/O-rich layers on Ru, respectively). As substitutions start forming Fe-Fe pairs, the energy cost increases due to the large value of W_i. This finding rationalizes the low optimal Fe content of the O-rich layers on Pt displayed in Fig.5.

Included in the effective parameters W_i is a magnetic contribution due to Fe-Fe interactions. When two Fe cations are first neighbors, their spins couple anti-ferromagnetically via a super-exchange mechanism, involving virtual excitations on the bridging oxygen atom. This coupling energy E_{AF} favors Fe-Fe first neighbor configurations. It gives a positive contribution to W_1, and thus acts toward phase separation. It is negligible when the two Fe cations are located further away. We find that E_{AF} is roughly similar in the four mixed layers, and amounts to $\approx +0.3$ eV. The magnetic interaction therefore does not discriminate the W_i values in the four systems, nor does it explain the global negative values of the W_i.

A second contribution to W_i comes from direct or oxygen-mediated non-magnetic interactions. Among them, as discussed in our previous works [34, 35], electrostatic interactions provide a strong negative contribution, due to the charge difference between the V and Fe cations. In O-poor layers, although the layer stoichiometry might suggest similar 3+ oxidation states for both V and Fe cations, the electron transfer to the substrate (stronger for the more electronegative Pt surface) allows a higher V oxidation state. The V oxidation state is also higher in the O-rich layers due to the high oxygen content. However, this negative

Table 2. Top part: Energy cost (eV) δE_1 and δE_2 to approach two Fe cations in first or second neighbor positions with AF spin coupling. Bottom part: Values (eV) of the mixing parameters W_1 and W_2, the magnetic Fe-Fe first neighbor interaction E_{AF} and the site energy ΔE (see text).

	O-poor/Pt	O-rich/Pt	O-poor/Ru	O-rich/Ru
δE_1	0.48	0.77	0.48	0.89
δE_2	0.13	0.55	0.10	-0.06
W_1	-0.42	-0.58	-0.44	-0.29
W_2	-0.04	-0.18	-0.05	0.03
E_{AF}	0.30	0.30	0.23	0.30
ΔE	0.03	0.19	0.04	0.64

electrostatic contribution is likely similar in the four mixed layers, and cannot explain the high W_1 and W_2 values in the O-rich layers on Pt, for example.

Implicitly included in the W_i values is the response of the substrates to the formation of Fe-Fe pairs upon approaching two Fe atoms by V-Fe exchange. Formally such a Fe-Fe pair may be considered as a negatively charged defect because it involves Fe cations of lower oxidation state than the V ones. With respect to the surrounding charge distribution, it has to be locally screened by the substrate. In O-poor layers, the two substrates are negatively charged, due to the electron transfer from the vanadium atoms. The formation of Fe-Fe pairs only diminishes this negative charge (in absolute value) without changing its sign, which does not cost much energy because of the electronegative character of the two substrates. However, due to their high oxygen content, things are different in the O-rich layers, under which the substrates are positively charged. As the local Fe content increases, this positive charge increases. It is not crucial on Ru which has a high oxygen affinity and is able to efficiently accommodate the positive charge by increasing its oxidation states (possibly up to +4 as in RuO_2), and/or by forming stronger Ru-O bonds across the interface. But oxidation of Pt is more difficult, due to its high electronegativity and as witnessed by the low stability of platinum oxides. The energy cost related to the positive charging of the metal substrate thus appears as the driving force which limits the Fe content in the mixed O-rich films on Pt.

6. Conclusion

Well-defined crystalline 2D mixed V-Fe oxide films with different ratios of the two cations and different oxygen contents have been successfully synthesized on Pt(111) and Ru(0001) substrates and characterized with atomically resolved STM experiments. With the help of DFT calculations, their relative stability has been analyzed and their mixing characteristics have been critically discussed.

We find that the mixed oxide layers under consideration display quite different stability characteristics. On the Ru substrate, which has a high affinity to oxygen, O-rich layers are favored in nearly the whole range of oxygen conditions, due to their strong interaction with the metal surface. As a consequence, the stability range of O-poor layers is limited to inaccessibly O-poor environments. In contrast, on the Pt surface, O-poor and O-rich films have a similar stability and coexist at the surface. Mixed V-Fe phases with close to 50% Fe content are systematically predicted to be the most stable at experimental oxygen conditions. Only in the O-rich layers on Pt the optimal Fe content is much smaller due to stronger Fe-Fe repulsion.

Mixing characteristics in the various oxide phases have been analyzed from the energy cost to approach two Fe atoms. This strategy departs from the traditional way of quantifying mixing properties due to the structural and compositional flexibility of these 2D mixed oxide layers under changing thermodynamic conditions. We find that in all the mixed systems, Fe-V first neighbor pairs are favored. A strong site effect in the O-rich layers on Ru reinforces the preference for mixing, while visibly stronger mixing parameters in the O-rich layers on Pt oppose substantial introduction of Fe atoms in the layers.

7. Acknowledgment

Financial support from the DFG grant Ni 650-5/2 'Functionalization of Cuprous Oxide: From Tailoring the Optical Response to Cu-based Ternary Oxide Materials' is gratefully acknowledged

8. Data availability statement

The data that support the findings of this study are available upon reasonable request from the authors.

9. Supporting Information Available

The Supporting Information contains: (1) large scale STM images; (2) calculated structures of metal-supported mixed $VFeO_n$ honeycomb films with various

oxygen contents; (3) simulated STM images of the observed mixed (V,Fe) oxide films.

This material is available free of charge via the Internet at http://pubs.acs.org.

10. References

[1] Lorenz M, Rao M R, Venkatesan T, Fortunato E, Barquinha P, Branquinho R, Salgueiro D, Martins R, Carlos E, Liu A *et al.* 2016 *Journal of Physics D: Applied Physics* **49** 433001

[2] Coll M, Fontcuberta J, Althammer M, Bibes M, Boschker H, Calleja A, Cheng G, Cuoco M, Dittmann R, Dkhil B *et al.* 2019 *Applied surface science* **482** 1–93

[3] Bibes M and Barthelemy A 2007 *IEEE transactions on electron devices* **54** 1003–1023

[4] Védrine J C 2017 *Catalysts* **7** 341

[5] Pacchioni G and Valeri S 2012 *Oxide ultrathin films: science and technology* (John Wiley & Sons)

[6] Netzer F P and Fortunelli A 2016 *Oxide materials at the two-dimensional limit* vol 234 (Springer)

[7] Netzer F P and Noguera C 2021 *Oxide Thin Films and Nanostructures* (Oxford University Press)

[8] Kresse G, Schmid M, Napetschnig E, Shishkin M, Köhler L and Varga P 2005 *Science* **308** 1440–1442

[9] Dai Z, Alyabyeva N, Van den Bossche M, Borghetti P, Chenot S, David P, Koltsov A, Renaud G, Jupille J, Cabailh G *et al.* 2020 *Physical Review Materials* **4** 074409

[10] Ly T T, Lee T, Kim S, Lee Y J, Duvjir G, Jang K, Palotás K, Jeong S Y, Soon A and Kim J 2019 *The Journal of Physical Chemistry C* **123** 12716–12721

[11] Möller C, Fedderwitz H, Noguera C, Goniakowski J and Nilius N 2018 *Physical Chemistry Chemical Physics* **20** 5636–5643

[12] Li F, Parteder G, Allegretti F, Franchini C, Podloucky R, Surnev S and Netzer F 2009 *Journal of Physics: Condensed Matter* **21** 134008

[13] Schoiswohl J, Sock M, Eck S, Surnev S, Ramsey M, Netzer F and Kresse G 2004 *Physical Review B* **69** 155403

[14] Barcaro G, Agnoli S, Sedona F, Rizzi G A, Fortunelli A and Granozzi G 2009 *J. Phys. Chem. C* **113** 5721–5729 ISSN 1932-7447

[15] Sun Y N, Giordano L, Goniakowski J, Lewandowski M, Qin Z H, Noguera C, Shaikhutdinov S, Pacchioni G and Freund H J 2010 *Angew. Chem. Int. Ed.* **49** 4418

[16] Giordano L, Lewandowski M, Groot I M N, Sun Y N, Goniakowski J, Noguera C, Shaikhutdinov S, Pacchioni G and Freund H J 2010 *Journal of Physical Chemistry C* **114** 21504–21509 ISSN 1932-7447

[17] Zeuthen H, Kudernatsch W, Peng G, Merte L R, Ono L K, Lammich L, Bai Y, Grabow L C, Mavrikakis M, Wendt S *et al.* 2013 *The Journal of Physical Chemistry C* **117** 15155–15163

[18] Merte L R, Shipilin M, Ataran S, Blomberg S, Zhang C, Mikkelsen A, Gustafson J and Lundgren E 2015 *The Journal of Physical Chemistry C* **119** 2572–2582

[19] Fester J, Sun Z, Rodriguez-Fernandez J and Lauritsen J V 2019 *The Journal of Physical Chemistry C* **123** 17407–17415

[20] Vasala S and Karppinen M 2015 *Progress in solid state chemistry* **43** 1–36

[21] Šutka A and Gross K A 2016 *Sensors and Actuators B: Chemical* **222** 95–105

[22] Zhu Y, Tahini H A, Hu Z, Dai J, Chen Y, Sun H, Zhou W, Liu M, Smith S C, Wang H *et al.* 2019 *Nature communications* **10** 1–9

[23] Stacchiola D, Kaya S, Weissenrieder J, Kuhlenbeck H, Shaikhutdinov S, Freund H J, Sierka M, Todorova T K and Sauer J 2006 *Angewandte Chemie International Edition* **45** 7636–7639

[24] Jerratsch J F, Nilius N, Freund H J, Martinez U, Giordano L and Pacchioni G 2009 *Physical Review B* **80** 245423

[25] Maria Zollner E, Schuster F, Meinel K, Stötzner P, Schenk S, Allner B, Förster S and Widdra W 2020 *physica status solidi (b)* **257** 1900655

[26] Wu C, Castell M R, Goniakowski J and Noguera C 2015 *Phys. Rev. B* **91** 155424

[27] Förster S, Meinel K, Hammer R, Trautmann M and Widdra W 2013 *Nature* **502** 215–218

[28] Lockhorn M, Kasten P E, Tosoni S, Pacchioni G and Nilius N 2019 *The Journal of chemical physics* **151** 234708

[29] Doudin N, Pomp S, Blatnik M, Resel R, Vorokhta M, Goniakowski J, Noguera C, Netzer F and Surnev S 2017 *Surface Science* **659** 20–30

[30] Sun Z, Rodríguez-Fernández J and Lauritsen J V 2022 *Journal of Physics: Condensed Matter* **34** 164004

[31] Goniakowski J and Noguera C 2019 *J. Phys. Chem. C* **123** 7898–7910

[32] Goniakowski J and Noguera C 2019 *J. Phys. Chem. C* **123** 9272–9281

[33] Goniakowski J and Noguera C 2020 *The Journal of Physical Chemistry C* **124** 8186–8197

[34] Wemhoff P I, Nilius N, Noguera C and Goniakowski J 2022 *The Journal of Physical Chemistry C* **126** 5070–5078

[35] Wemhoff P I, Noguera C, Goniakowski J and Nilius N 2022 *The Journal of Physical Chemistry C* **126** 19947–19955

[36] Kresse G and Furthmuller J 1996 *Phys. Rev. B* **54** 11169–11186

[37] Kresse G and Hafner J 1993 *Phys. Rev. B* **47** 558–561

[38] Blöchl P E 1994 *Phys. Rev. B* **50** 17953–17979

[39] Kresse G and Joubert D 1999 *Phys. Rev. B* **59** 1758–1775

[40] Dion M, Rydberg H, Schroder E, Langreth D C and Lundqvist B I 2004 *Phys. Rev. Lett.* **92** 246401

[41] Klimes J, Bowler D R and Michaelides A 2010 *J. Phys.: Cond. Matt.* **22** 022201

[42] Klimes J, Bowler D R and Michaelides A 2011 *Phys. Rev. B* **83** 195131

[43] Anisimov V I, Aryasetiawan F and Liechtenstein A I 1997 *J. Phys.: Condens. Matter* **9** 767–808

[44] Dudarev S L, Botton G A, Savrasov S Y, Humphreys C J and Sutton A P 1998 *Phys. Rev. B* **57** 1505–1509

[45] Le H L T, Goniakowski J and Noguera C 2018 *Phys. Rev. Mat.* **2** 085001

[46] Le H L, Goniakowski J and Noguera C 2019 *Surface Science* **679** 17–23

[47] Bader R F W 1991 *Chem. Rev.* **91** 893–928

[48] Henkelman G, Arnaldsson A and Jonsson H 2006 *Comput. Mater. Sci.* **36** 354–360

[49] Momma K and Izumi F 2011 *J. Appl. Crystallogr.* **41** 1272–1276

[50] Monkhorst H and Pack J 1976 *Phys. Rev. B* **13** 5188–5192

[51] Wang Y, Wemhoff P I, Lewandowski M and Nilius N 2021 *Physical Chemistry Chemical Physics* **23** 8439–8445

[52] Ducastelle F 1991 *Order and Phase Stability in Alloys.* (Elsevier)

[53] Allan N, Barrera G, Fracchia R, Lavrentiev M Y, Taylor M, Todorov I and Purton J 2001 *Physical Review B* **63** 094203

[54] Vinograd V L, Winkler B, Putnis A, Gale J D and Sluiter M H 2006 *Chemical Geology* **225** 304–313

[55] Noguera C and Fritz B 2017 Solid solution/exsolution *Encyclopedia of Geochemistry: A Comprehensive Reference Source on the Chemistry of the Earth* ed White W M (Cham: Springer International Publishing) pp S:1–8

[56] Ketteler G and Ranke W 2003 *The Journal of Physical Chemistry B* **107** 4320–4333

[57] Palacio I, Monti M, Marco J F, McCarty K F and de la

Figuera J 2013 *Journal of Physics: Condensed Matter* **25** 484001

[58] Ossowski T, Wang Y, Carraro G, Kiejna A and Lewandowski M 2022 *Journal of Magnetism and Magnetic Materials* **546** 168832